

# Imaging Geostationary Satellites with a Common-Mount Interferometer: Image quality and fringe tracking

Anders M. Jorgensen<sup>a</sup>, H. R. Schmitt<sup>b</sup>, D. Mozurkewich<sup>c</sup>, J. T. Armstrong<sup>b</sup>,  
R. L. Hindsley<sup>b</sup>, E. K. Baines<sup>b</sup>

<sup>a</sup>New Mexico Institute of Mining and Technology, Socorro, NM, USA

<sup>b</sup>Naval Research Laboratory, Washington, DC, USA

<sup>c</sup>Seabrook Engineering, Seabrook, MD, USA

## ABSTRACT

Imaging geostationary satellites is difficult because they are both too large and too small. They are too small to resolve with existing ground-based single telescopes, and they are too large (and too faint) to resolve with existing ground-based interferometers. Earth-rotation synthesis also does not work with geostationary satellites. We have designed a common-mount telescopes which we believe is the right instrument for geostationary satellite imaging, and described it previously in a number of publications (e.g. AMOS papers Mozurkewich et al. 2011, Jorgensen et al. 2011, Schmitt et al. 2011, and others). In this paper we will provide an overview of the instrument and explore its capabilities in more detail, using a typical geostationary satellite as an example. Specifically we will look at the fringe-tracking capability which is required for phase measurement and thus imaging. We will also look at the required integration time and its relationship to fringe-tracking capability and image quality.

## 1. INTRODUCTION

While the U.S. has telescopes around the world capable of imaging objects in low-Earth orbit (LEO), the capability to image high-altitude satellites in the visible and near-infrared still does not exist, and is needed to support the Space Situational Awareness (SSA) mission. GEO satellites are typically very large, very high value, sometimes exceeding  $> \$10^9$ , providing essential military and civilian communications services (such as satellite TV signal and other communications). In previous papers<sup>1,2</sup> we discussed the possibility of imaging satellites with astronomical interferometers. Recently we introduced the imaging of geostationary satellites with a common mount interferometer consists of thirty 1.4 m telescopes on a common mount.<sup>3-7</sup> In this paper we extend the analysis of the common-mount interferometer.

Geostationary satellites have a size of a few 10s of m, and the desired resolution is often a fraction of a m.<sup>1,2,8</sup> To achieve the desired resolution with a single-dish telescope would require a diameter of several 10s of m to close to 100 m. Such a large telescope would be extremely expensive, would require a very sophisticated adaptive optics system, and would be overkill in terms of its photon collection capability.

An alternative is to use a interferometer. We propose a common-mount interferometer which involves a large number of individual telescopes mounted on a single steerable platform. There are several advantages to

this, including that it eliminates the need for long delay lines, and eliminates the need for mounts on the individual telescopes. That in turn reduces complexity and allows for the telescopes to be placed closer together to achieve shorter baselines which are necessary for geostationary satellite imaging.<sup>1</sup>

Geostationary satellites are also faint. Their median brightness is  $V=13.5$ , with some as bright as  $V=10$  and a few fainter than  $V=15$ .<sup>2,9</sup> That satellites are faint and large poses fringe-tracking and imaging SNR questions which must be explored. We do that in this paper.

The Navy Precision Optical Interferometer<sup>10</sup> (NPOI) has demonstrated the phasing of an optical baseline on a GEO source using a specular reflection of sunlight from the source.<sup>8,11,12</sup> The Magdalena Ridge Observatory Interferometer (MROI) has been proposed as a satellite imaging interferometer because of its planned short baselines and large apertures.<sup>2,13</sup> While MROI is expected to track fringes on targets as faint as geostationary satellites, both NPOI and MROI suffer from baselines which are too long for optimal tracking on the very large satellite objects.<sup>1</sup> NPOI has the capability for much shorter baselines, but has smaller apertures with limited light collection. MROI cannot observe shorter baselines because of the size of telescopes and their enclosures.

The Geo Light Imaging National Testbed<sup>14</sup> (GLINT) is an imaging concept in which the geostationary satellite is flood illuminated by 3 lasers simultane-

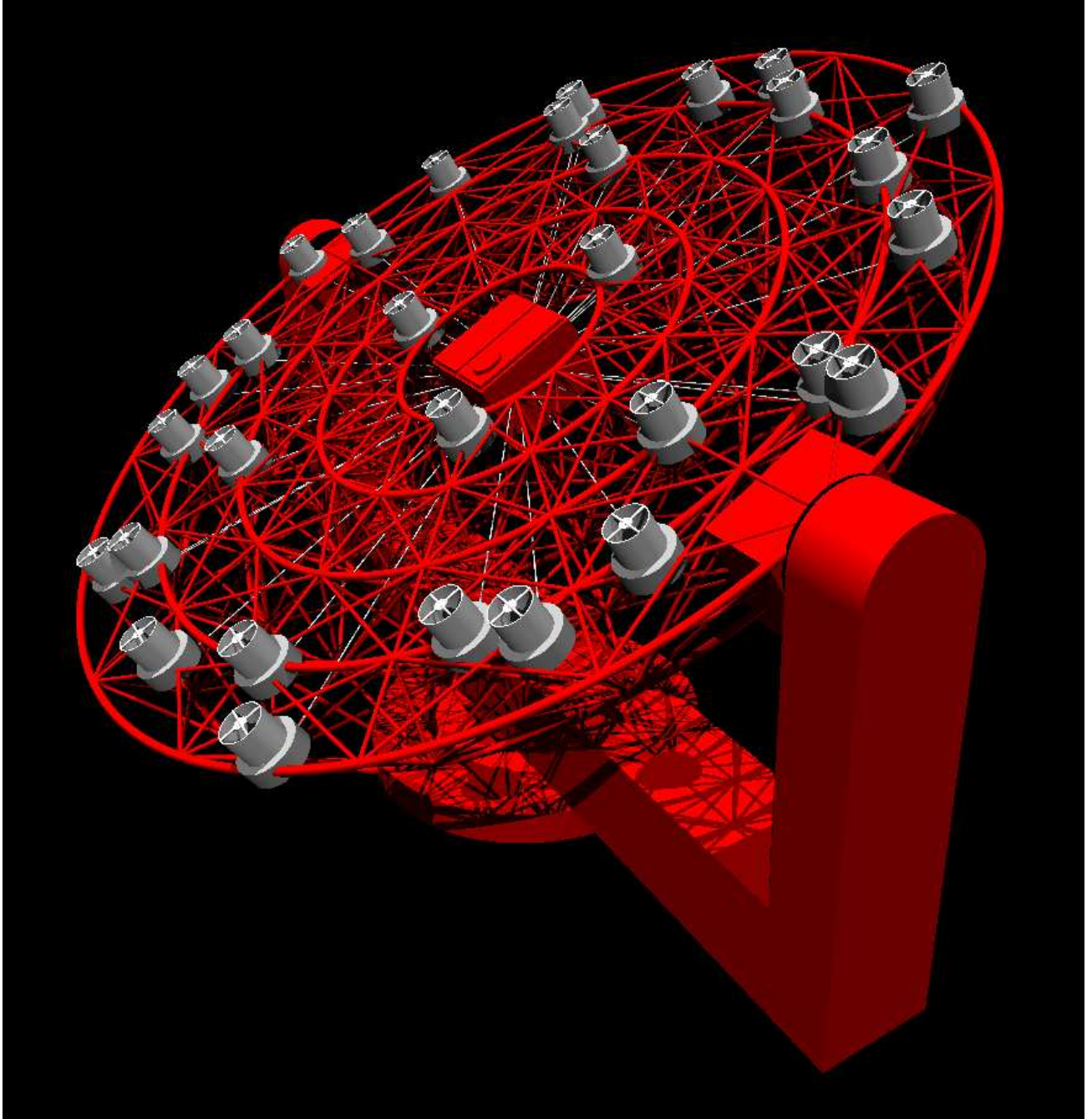


**Figure 1.** Three-dimensional model of the instrument. 30 telescopes are mounted on an Alt-Az platform. In the model the individual telescopes can be seen, as well as the fiber relay pipes to the combiner room, and the combiner room.

ously. Pairs of these lasers are tagged with a frequency offset such that the satellite is scanned in 2 dimensions by the fringe pattern formed by the laser irradiance at the satellite. The resulting scan modulation generates a closure phase which can be read by a simple photo detector on the ground. The GLINT concept did not

proceed to system level testing.

## 2. INSTRUMENT DESCRIPTION

The instrument that we propose is depicted in Figure 1. It consists of a single mount with a size of approximately 50 m (depending on the desired resolution) and

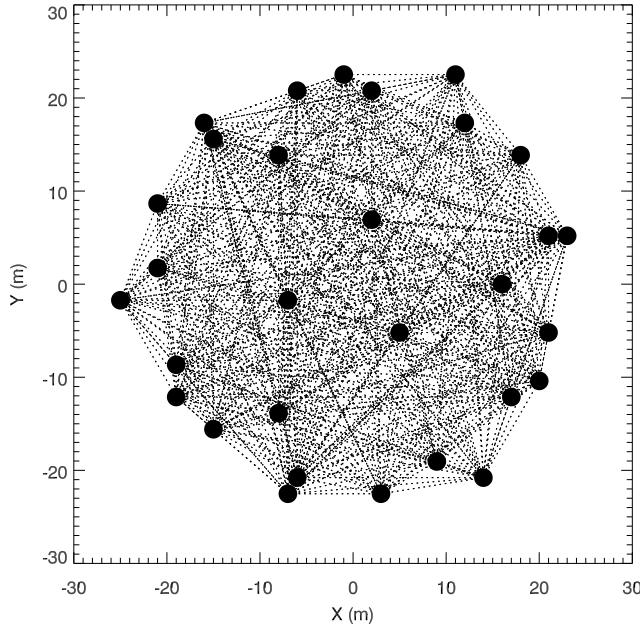


**Figure 2.** Map of stations and baselines for the array layout used in this paper.

approximately 30 telescopes each with a diameter of 1.4 m (depending on the desired sensitivity). In this concept V-band light is used for the wavefront sensor to phase the large mirrors, H-band light is used for fringe-tracking, and the imaging is carried out in the R-band. The instrument and optics are described in detail in a separate paper.<sup>3</sup>

The telescopes are laid out in a non-redundant array configuration, shown in Figure 2 together with all possible 435 baselines. The light from the telescopes is fed into fibers which transport it to the beam combiner at the center of the telescope. This design has a small number of mirrors and high throughput. Very importantly, the design involves no long delay lines, and no tracking mounts for the individual telescopes, which is likely to reduce the cost of the system, and which also makes it easier to install additional telescopes on the structure. Not having individual mounts on the telescopes also makes it possible to place them closer together to improve fringe-tracking performance. All 435 baselines can be observed simultaneously.

The fringe-tracking system (in H-band) and imaging systems (in R-band) are configured differently. For fringe-tracking it only makes sense to split the light between the baselines which have large SNR. For imaging we want all or most baselines. For combining all baselines there are two basic options, one involving pair-wise combination (thus splitting the light in 30), and

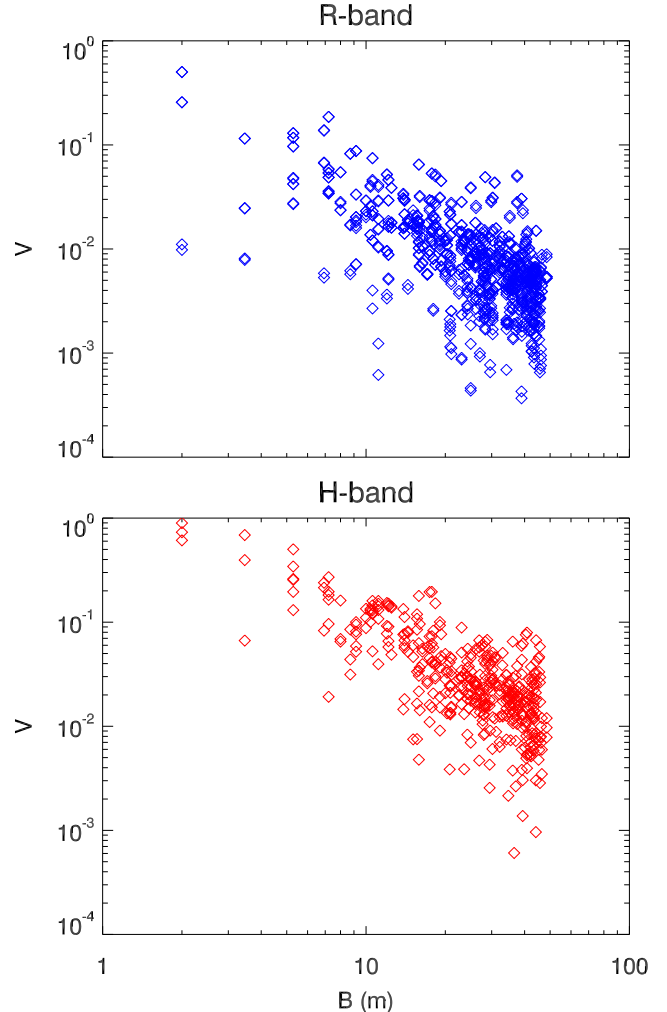


**Figure 3.** Visibilities as a function of baselines length in the R-band (top) and the H-band (bottom)

the other involving all-on-one combiner. The all-on-one combiner has slightly better SNR characteristics. We will however base our calculations on 435 pair-wise combinations because those calculations are straightforward.

### 3. FRINGE-TRACKING SNR

To evaluate the fringe-tracking capability of the instrument we simulated observations of a satellite named Gorizont. The satellite is described in more detail in separate papers.<sup>4,7</sup> We assume the satellite has a size of 15 m and simulate the visibilities that would be observed with the telescope on this satellite. Figure 3 plots the visibilities in the R-band and H-band as a function of baseline length. The longest baseline is almost 50 m. The top panel of Figure 3 shows the visibilities in

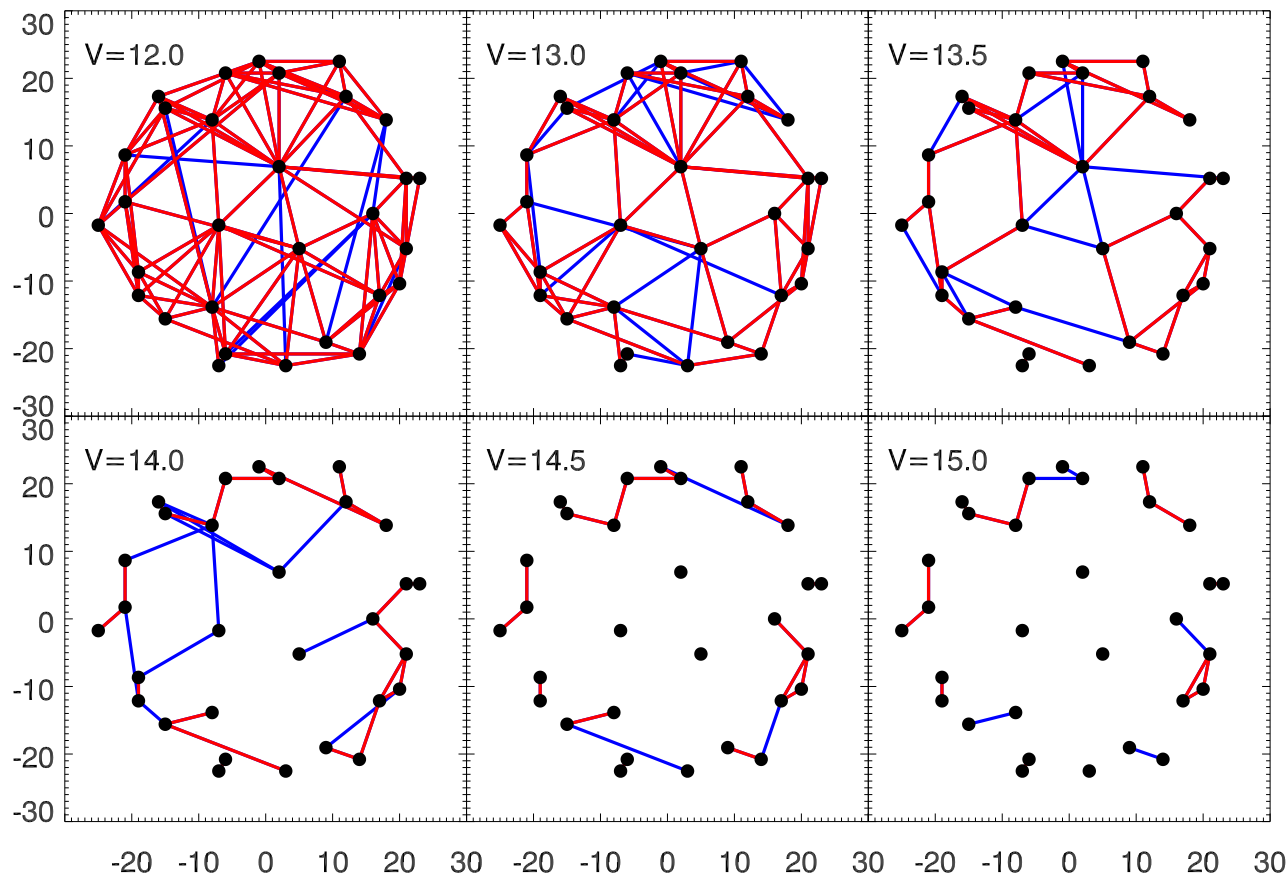


**Figure 4.** Maps of tracking baselines in H-band at different V-band magnitudes. Blue corresponds to  $7 < \text{SNR} < 10$  and red corresponds to  $\text{SNR} > 10$ . For  $V = 12$  a large number of baselines are able to track at  $\text{SNR} > 10$ . For  $V = 15$  only a few baselines are able to track.

the R-band and the bottom panel the visibilities in the H-band.

In order to be able to record fringe observations it is necessary to phase the array of telescopes. To do this a sufficiently large number of baselines, ideally baselines which continuously connect all baselines, must have sufficiently large SNR. It is generally accepted that a SNR of several across the entire band in one atmospheric coherence time is necessary for fringe-tracking.

The necessary calculations are described in our 2011 AMOS paper in section 3<sup>5</sup> and we make use of them here. The fringe-tracking SNR is defined as

$$\text{SNR}_T = NV^2 \quad (1)$$

where  $N$  is the number of photons recorded in two atmospheric coherence times and  $V$  is the visibility amplitude. Using the same assumptions as in our previous paper we compute the SNR on each baseline as a

function of the satellite magnitude. Then we look at how many of the baselines have a minimum SNR. In Figure 4 we show, in blue, the baselines which have  $7 < \text{SNR} < 10$  and, in red,  $\text{SNR} > 10$ . The conclusion is that the fringe-tracking limit appears to be between  $V = 14$  and  $V = 15$ .

Figure 5 shows the number of stations which are connected to a tracking baseline. This gives an approximate measure of the ability to phase the array. The left panel is for R-band fringe-tracking and the right panel is for H-band tracking. The blue curve is for  $7 < \text{SNR} < 10$  and the red curves is for  $\text{SNR} > 10$ . The plots show that fringe-tracking in the R-band is significantly less effective than in the H-band. Also, in the H-band all stations are connected to a tracking baseline up to approximately  $V = 14$ . Beyond that tracking is lost on some stations, and by approximately  $V = 15$  one third of stations are no longer tracking.

The practical fringe-tracking limit appears to be be-

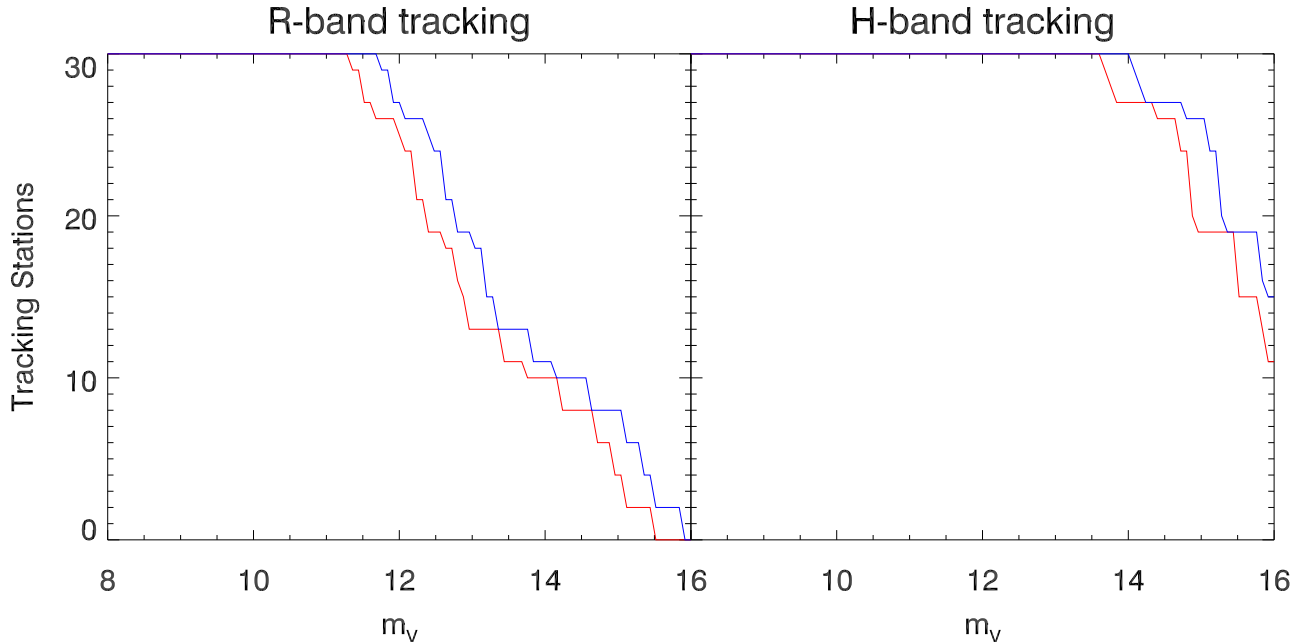


**Figure 5.** Number of stations connected to a tracking baseline as a function of V-band magnitude. The left-panel is for fringe-tracking in the R-band and the right panel is for fringe-tracking in the H-band. Blue curves are for  $\text{SNR} > 7$ , and red is for  $\text{SNR} > 10$ .

tween  $V = 14$  and  $V = 15$ . This will cover the majority of geostationary satellites which have a median V-band magnitude of approximately  $V = 13.5$ .

#### 4. IMAGING INTEGRATION TIME

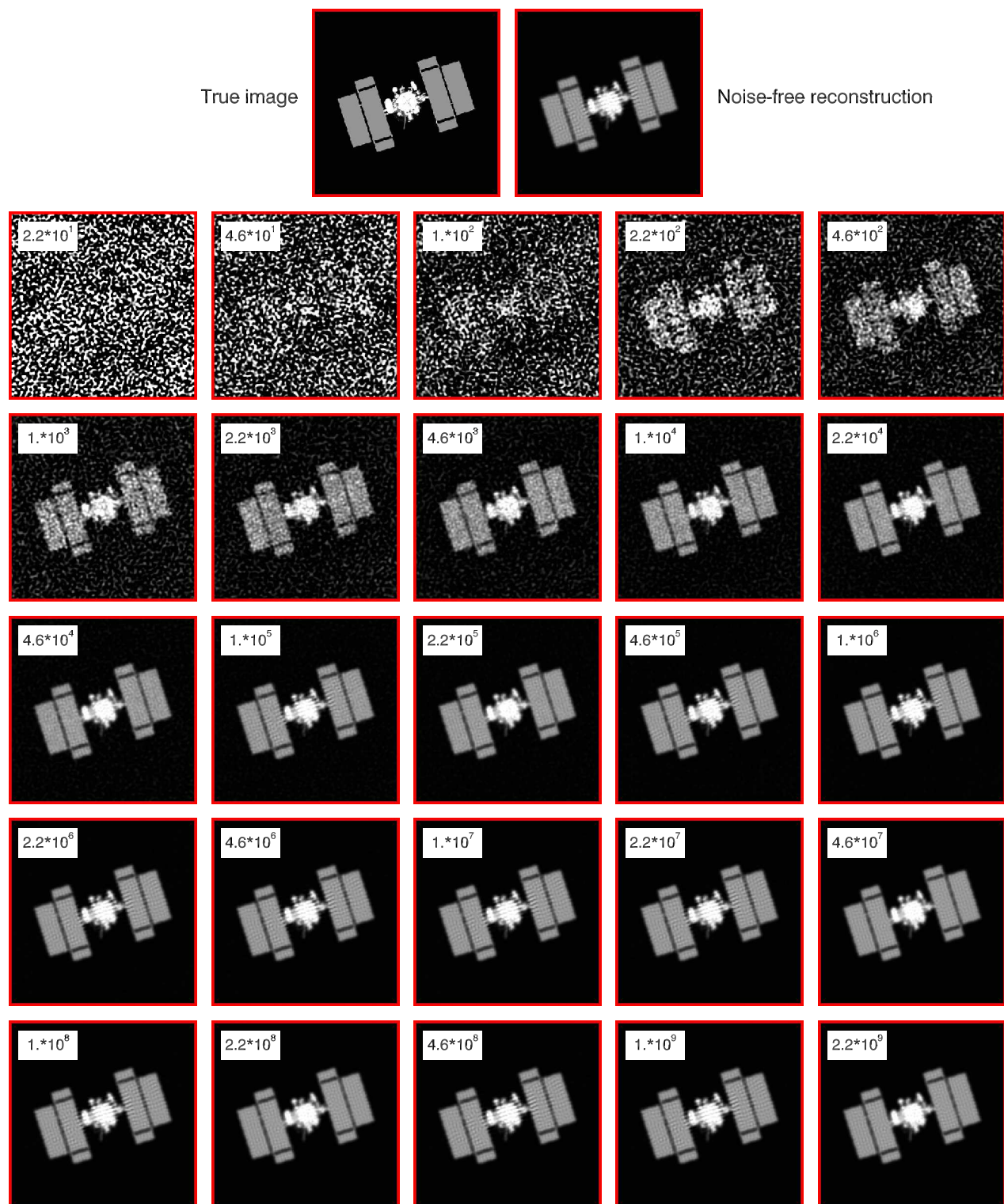
The imaging capability is limited by two factors. One is the UV-coverage of the telescope array, and another is the SNR of the individual visibilities due to photon counting noise. Longer integration time will improve the image quality, but because of the UV-coverage limit the images will never fully reproduce the object. We think that it is reasonable to define a optimal imaging time to be the time at which the image quality transitions from being dominated by photon noise to being dominated by UV-coverage.

Figure 6 shows, in the top row, on the left side, the original true image of the satellite. This is the image used to simulate visibilities. On the right is the reconstructed image using noise-free (infinite SNR) visibilities. The next 25 images are for increasing SNR, starting at 20 photons per baseline and ranging up to  $2 \times 10^9$  photons per baseline. The solar panels can just be distinguished at 100 or 200 photons, and it appears to require  $10^4$  photons to reach full accuracy on the satellite body and  $10^5$  photons to reach full accuracy on the solar panels.

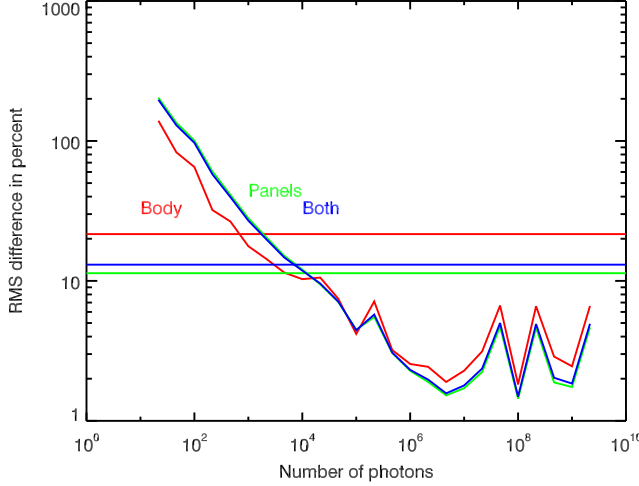
However, rather than relying on subjective visual inspection of the images to determine whether they are good enough, let us develop a quantitative measure. The quantitative measure is the normalized RMS mean difference between pixels in two images. This difference is measured in percent brightness difference (normalized by the true image brightness) between the same image pixel in two different images. We will compare the photon noise limited images, the zero-noise reconstructed image, and the true original image.

Figure 7 shows this comparison. We divide the image into several components, the satellite body (white in the top left image of Figure 6), the solar panels (gray color in the top left image of Figure 6), and the combined body and panel pixels. Whether a pixel belongs to one of the three groups, and which one, is determined from the original image. Then Figure 7 shows this metric for all the images in Figure 6. The color coding is red for the body, green for the solar panels, and blue for either body or panels. The horizontal lines are the RMS difference between the original image and the noise-free reconstructed image. We can see that for the body the RMS brightness difference between the true and reconstructed images is approximately 20%. For the panels it is closer to 10%. The three colored curves are then the RMS differences between the noise-free image and the bottom 25 images which have photon noise, in Figure 6. We think that the flattening of the three colored





**Figure 6.** Images of the Gorizont satellite. In the top row the left image is the true image of the satellite, used to simulate visibilities. The left image is the reconstructed image with noiseless visibilities. The bottom 25 images are from left to right then top to bottom reconstructed images with increasing number of photons from 20 to  $2 \times 10^9$  per baseline. The image of the satellite is visible after 200 photons and beyond about  $10^4$  photons there appears to be little visible improvement in the body. After  $10^5$  there does not appear to be any improvement in the image quality of the solar panels.



**Figure 7.** Image RMS differences as a function of the number of photons in the images from Figure 6. The pixels in the original true image are divided into groups according to whether they belong to the white satellite body (red color), the gray solar panels (green color), or either the body or the panels (blue color). The horizontal curves are the difference between the noise-free reconstructed image and the original true image. The other curves are the differences between the noise-free image and the images with different number of photons per baseline. The crossing point of the horizontal line and curve of the same color represents the optimal number of photons required for imaging.

curves at higher photon rate is related to limitations in the image reconstruction software (we used AIPS).

According to the previous discussion in this section the optimal integration time is then the point at which the curve and horizontal line of the same color cross. For the satellite body, the red curve,  $6.9 \times 10^2$  photons are required per baseline. For the solar panels it takes  $12 \times 10^3$  photons per baseline and for the whole satellite  $7 \times 10^3$  photons per baseline. We can convert these photon counts into integration times for satellites of different magnitude, which we consider next.

Figure 8 plots the relationship between satellite magnitude and integration time for different levels of uncertainty in the visibilities. Because the uncertainty in  $V$ ,  $\sigma_V$ , is directly related to the visibility through

$$\text{SNR}_I = \frac{V}{\sigma_V} = \sqrt{N}V \quad (2)$$

it is a simple matter of converting. This plot shows, for example, that to achieve  $\sigma_V = 0.003$  for a satellite with V-band magnitude of 12 requires approximately 300 s of integration time. This also corresponds to 83% of the visibilities having  $\text{SNR} > 1$ .

On Figure 8 is also plotted, in color, the integration time as a function of visual magnitude corresponding to

the three different number photons per baseline that we found in Figure 7. Thus, the optimal integration time to image the satellite body of a visual magnitude 14 satellite is only a little more than 10 s, whereas for the solar panels it is 4 minutes. For a 15th magnitude satellites the numbers are a half minute and approximately 10 minutes, respectively. It is somewhat surprising that all of these cases correspond to the majority of visibilities having a SNR of less than unity. However, a large number of sub-unity SNR visibilities can still contribute useful information to the imaging.

## 5. DISCUSSION

The common-mount interferometer has several advantages over a traditional array of individual telescopes. Only a single mount is required, such that the individual telescopes can be made less expensive and more can be used. Additionally, the ability to point the entire array reduces the need for long delay lines which makes fibers and fiber-stretching more practical. That in turn reduces the number of reflections and the light-loss on the way to the beam combiner.

In analyzing the fringe-tracking capability we found that the H-band is much better than the R-band for fringe-tracking. The interferometer is in-fact designed to fringe-track in the H-band, control the adaptive optics in the V-band, and image in the R-band. It may be possible to further improve the fringe-tracking by taking advantage of unused bands, such as K-band. The fringe-tracking appears to be limited to somewhere between 14th and 15th magnitude. There are several ways to improve this. One possible option is to use larger telescopes than the 1.4 m telescopes envisioned. Another option is to add a few additional telescopes to shorten some of the longest tracking baselines which limit the fringe-tracking capability. Yet another way may be to explore re-arranging the telescopes to shorten the longest of the tracking baselines, or to use a partially redundant array. However doing the latter will eliminate the possibility of an all-on-one combiner.

For the imaging capability it appears that the quantitative measure indicates a smaller number of photons needed than the visual inspection. It may be that the integration times in Figure 8 are a underestimate, perhaps by a factor of 5, compared to the visual inspection of the images. If we increase the integration time and rely on the solar panel metric, which produces the longest integration time, then it takes 20 minutes to image a 14th magnitude satellite. It will then take 4 minutes to image a 13th magnitude satellite and about

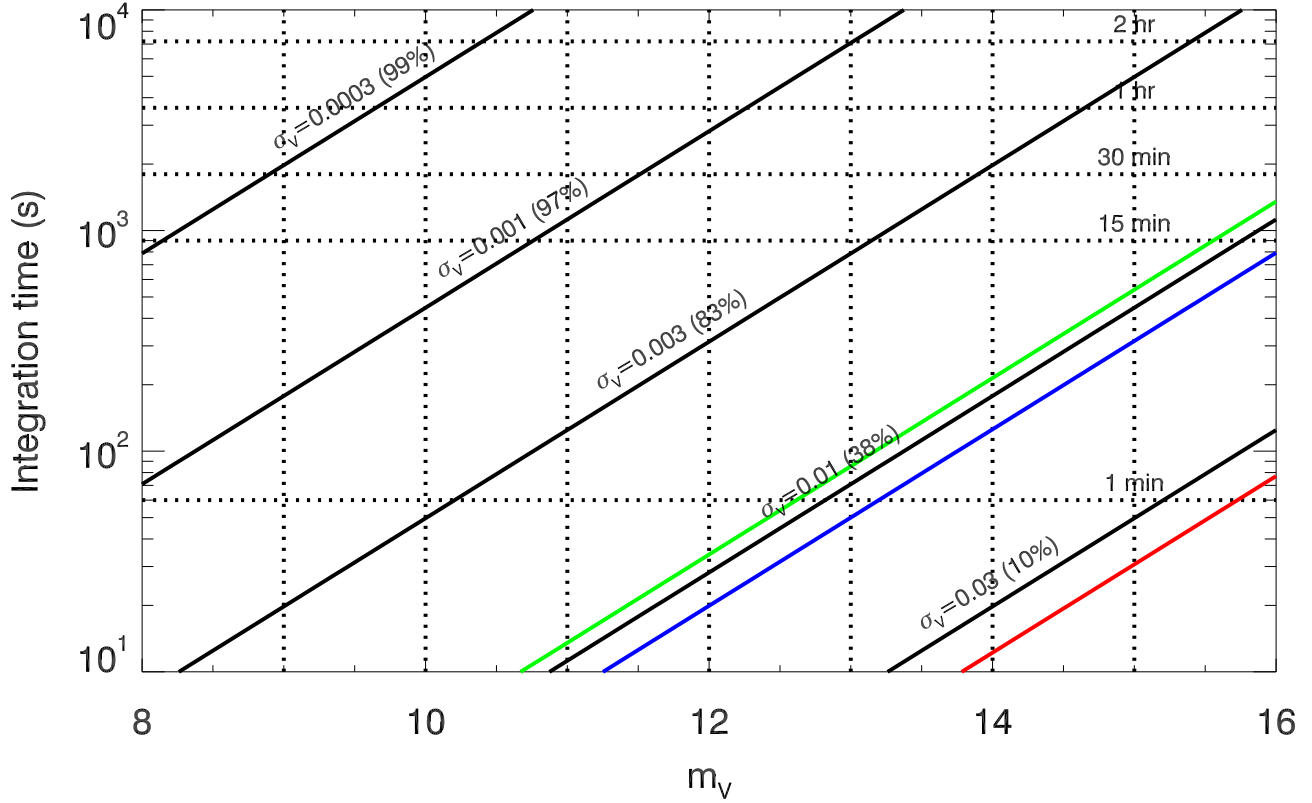


**Figure 8.** Integration time as a function of magnitude. For a given visibility amplitude uncertainty there is a linear relationship between the the visible magnitude and the log of the integration time. The colored lines correspond to optimal number of photons required, from Figure 7.

an hour to image a 15th magnitude satellite. All of these integration times are still acceptable.

## 6. CONCLUSION

This paper presents additional analysis of the common-mount interferometer that we introduced in three papers at AMOS 2011. The common-mount interferometer is capable of imaging the majority of geostationary satellites in a brief snapshot imaging mode.

We have shown that the interferometer is capable of fringe-tracking on satellites to somewhere between 14th and 15th magnitude, and produce images of these faint satellites after integration times that last from a few minutes to an hour for the faintest 15th magnitude satellites. This makes it possible to produce images of several to many geostationary satellite within the field of view of the telescope each night.

We have also suggested that some improvements can push the faint magnitude limit a little bit further to increase the fraction of satellites that can be observed.

## REFERENCES

1. A. M. Jorgensen, H. Schmitt, J. T. Armstrong, D. Mozurkewich, E. Baines, R. Hindsley, D. Hutter, and S. Restaino, "Coherent integration results from the NPOI," in Proceedings of the SPIE meeting Astronomical Telescopes and Instrumentation, 2010.
2. E. J. Bakker, D. A. Klinglesmith, A. M. Jorgensen, D. Westpfahl, V. Romero, and C. Cormier, "Imaging of geostationary satellites with the MRO interferometer," in Proc. Advanced Maui Optical and Space Surveillance Technologies Conference, 2009.
3. D. Mozurkewich, J. T. Armstrong, R. B. Hindsley, A. M. Jorgensen, S. R. Restaino, and H. R. Schmitt, "Toward the ground-based imaging of satellites at geosynchronous altitude," in Proc. Advanced Maui Optical and Space Surveillance Technologies Conference, 2011.
4. H. R. Schmitt, D. Mozurkewich, S. R. Restaino, J. T. Armstrong, E. K. Baines, R. B. Hindsley, and A. M. Jorgensen, "Simulated synthesis imaging of geostationary satellites," in Proc. Advanced



- Maui Optical and Space Surveillance Technologies Conference, 2011.
5. A. M. Jorgensen, H. R. Schmitt, D. Mozurkewich, J. T. Armstrong, S. Restaino, and R. L. Hindsley, "Interferometric imaging of geostationary satellites: Signal-to-noise considerations," in Proc. Advanced Maui Optical and Space Surveillance Technologies Conference, 2011.
  6. D. Mozurkewich, J. T. Armstrong, R. B. Hindsley, A. M. Jorgensen, S. R. Restaino, and H. R. Schmitt, "An imaging interferometer for compact sources," in Proc. SPIE 8165, 2011.
  7. H. R. Schmitt, D. Mozurkewich, S. R. Restaino, J. T. Armstrong, E. K. Baines, R. B. Hindsley, and A. M. Jorgensen, "Simulated optical interferometric observations of satellites," in Proc. SPIE 8165, 2011.
  8. J. T. Armstrong, R. B. Hindsley, S. R. Restaino, J. A. Benson, D. J. Hutter, F. J. Vrba, R. T. Zavala, S. A. Gregory, and H. R. Schmitt, "Observations of a geosynchronous satellite with optical interferometry," in Proc. Advanced Maui Optical and Space Surveillance Technologies Conference, 2009.
  9. D. J. Sanchez, S. A. Gregory, D. K. Werling, T. E. Payne, L. Kann, L. G. Finkner, D. M. Payne, and C. K. Davis, "Photometric measurements of deep space satellites," in Proc. SPIE 4091, Imaging Technology and Telescopes, J. W. Bilbro, J. B. Breckinridge, R. A. Carreras, S. R. Czyzak, M. J. Eckart, R. D. Fiete, and P. S. Idell, eds., 2000.
  10. J. T. Armstrong, D. Mozurkewich, L. J. Rickard, D. J. Hutter, J. A. Benson, P. F. Bowers, N. M. E. II, C. A. Hummel, K. J. Johnston, D. F. Buscher, J. H. C. III, L. Ha, L.-C. Ling, N. M. White, and R. S. Simon, "The navy prototype optical interferometer," The Astrophysical Journal **496**, pp. 550–571, 1998.
  11. J. T. Armstrong, R. B. Hindsley, S. R. Restaino, R. T. Zavala, J. A. Benson, F. J. Vrba, D. J. Hutter, S. A. Gregory, H. R. Schmitt, J. R. Andrews, and C. C. Wilcox, "Observations of a geosynchronous satellite with optical interferometry," in Adaptive Coded Aperture Imaging, Non-Imaging, and Unconventional Imaging Sensor Systems II, S. Rogers, D. P. Casasent, J. J. Dolne, T. J. Karr, and V. L. Gamiz, eds., p. 78180L, 2010.
  12. J. T. Armstrong, R. B. Hindsley, H. R. Schmitt, F. J. Vrba, J. A. Benson, D. J. Hutter, and R. T. Zavala, "Detection of a geostationary satellite with the Navy Prototype Optical Interferometer," in Proc. Optical and Infrared Interferometry II, W. C. Danchi, F. Delplancke, and J. K. Rajagopal, eds., pp. 77343C–77343C–7, 2010.
  13. I. Payne, M. Creech-Eakman, V. Romero, D. Buscher, and C. Haniff, "The magdalena ridge observatory interferometer: Geostationary target imaging capabilities," in Proc. Advanced Maui Optical and Space Surveillance Technologies Conference, 2010.
  14. V. J. Gamiz, R. B. Holmes, S. R. Czysak, and D. G. Voelz, "GLINT: program overview and potential science objectives," in Proc. SPIE 4091, Imaging Technology and Telescopes, J. W. Bilbro, J. B. Breckinridge, R. A. Carreras, S. R. Czyzak, M. J. Eckart, R. D. Fiete, and P. S. Idell, eds., pp. 304–315, 2000.